Supporting Information

Ranitovic et al. 10.1073/pnas.1321999111

SI Text

In this supporting text, we first provide additional details about the experimental setup. Next, we provide additional data to explain in detail how the coupled electronic wave packet, IR laser interferences, and nuclear wave packet dynamics allow us control excitation and dissociation channels in D_2. Finally, we explain our fully quantum calculations that model the short timescale electronic wave packet interference dynamics in H_2. We also provide additional theory on the longer timescale dynamics that beautifully show that we can exquisitely control tunneling and oscillation in a double-well excited state neutral molecule potential, by tuning the high harmonic generation (HHG) photon energies and electronic wave packet interferences.

Experiment. Our experimental setup consists of a high-power (30 W), high repetition rate (10 kHz), 30-fs Ti:sapphire laser system (784 nm); a gas-filled waveguide for generating harmonics; and a cold target recoil ion momentum spectroscopy (COLTRIMS) apparatus that allows for simultaneous detection of ion and electron 3D momenta. Using part of the laser output, high harmonics (HHG) were generated in Xe gas and then refocused into a separate deuterated hydrogen (D_2) gas target using a pair of multilayer vacuum UV (VUV) mirrors that reflect photon energies up to 22 eV. (To achieve the maximum efficiency, the supersonic COLTRIMS D_2 jet was replaced with an effusive, thick target.) The exact energies of the harmonics can be continuously tuned by the phase-matching conditions via pressure tuning of Xe, as explained below. A small portion of the IR pulse that drives the HHG process copropagated with the VUV pulse. These two pulses (VUV/IR) with similar intensities were locked in phase to form one multicolor pump beam. The probe IR beam was delayed relative to the pump beam using a picomotor-driven delay stage. This VUV/IR interferometer was interferometrically stable to enable the interference of the electronic wave packets. The VUV and IR pulse durations were 10 and 30 fs, respectively, whereas the pump and probe IR pulse intensities were 3×10^{11} W/cm^2 and 4×10^{12} W/cm^2, respectively. All of the pulses were linearly polarized.

Fig. S1 is an extended version of Fig. 1 and shows in more detail ground and excited states of a deuterated hydrogen molecule (D_2 is the same as H_2). We also show the photoelectron, D^+, and D_2^+ yields, as well as kinetic energies of the electrons and the D^+ ions, for two different central wavelengths of the VUV frequency comb. The wavelength (photon energy) of the VUV harmonics was fine-tuned while keeping the driving and probing IR wavelengths unchanged by adjusting the Xe pressure (and thus the HHG phase-matching) in the gas-filled waveguide (1–3), as shown in Fig. S2. As the Xe pressure in the HHG waveguide was increased from 5 to 20 torr, the photoelectron energies that result from ionizing Ar by the VUV HHG comb also increased because it is possible to phase-match at slightly higher photon energies. This ability to fine-tune VUV photon energies allows us to distinguish between various excitation and control mechanisms.

Fig. 1*E* shows how this phase-matching approach allows for fine control of the periodicity of the e^-/D_2^+ yields that changes from full to half-optical cycle duration of the IR laser field, as the harmonic energies were blue-shifted. We also see from Fig. 1 that the periodicity of the D^+ yield does not depend on the VUV photon energy; this is expected because the excited molecule was ionized in the combined field of the two IR pump and probe pulses, which determines the periodicity observed in the ion yield. Thus, the phase of the D^+ oscillation provides a reference for the instantaneous value of the total electric field that drives the dissociation of the bound $1s\sigma_g$ nuclear wave packet [high kinetic energy release (KER) channel], as well as the dissociation through the low KER channel. Though the high KER channel originates from a bond-softening process, which is routinely observed in many strong-field processes, the low KER channel originates from direct dissociation of D_2 as the highly excited Rydberg states were ionized at larger internuclear separations by the tail of the two IR pulses.

Theory. Due to extremely lengthy and time-consuming theoretical calculations, we modeled pulses of duration 7.75 fs for time delays no longer than 10 fs. In this calculation, we used an electric field consisting of a combined VUV and IR pump field followed by an IR probe field. Both IR fields had a frequency $\omega = 1.6$ eV (775 nm) and were three cycles in duration. The pump IR pulse was phase-locked to the VUV pulse, with an intensity of 0.3×10^{12} W/cm^2. The probe IR pulse intensity was 5×10^{12} W/cm^2, corresponding to the estimated experimental IR intensities.

The VUV field consists of four pulses, with an intensity of 10^9 W/cm^2 for the two central pulses and 0.35×10^9 W/cm^2 for the other pulses, which corresponds to an envelope with FWHM = 3 fs and a laser intensity $I = 1.14 \times 10^9$ W/cm^2. To simulate the blue-shift effect of the experimental VUV pulses, we used the VUV combs with the central frequency corresponding to 9ω for three different IR wavelengths: 784, 760, and 740 nm (or 1.58, 1.63, and 1.68 eV photon energies). The delay between the (VUV + IR) pump and the IR probe pulses was scanned from −4 fs to 4 fs (the pump precedes the probe for positive time delays).

We solved the time-dependent Schrödinger equation (TDSE) for H_2 using a close-coupling method that includes the bound states; the $^2\Sigma_g^+(1s\sigma_g)$ and the $^2\Sigma_u^+(2p\sigma_u)$ ionization continua; and the doubly excited states embedded in them. The method is similar to that described in refs. 4–6 and used in refs. 7 and 8. The calculations consider all electronic and vibrational degrees of freedom, as well as the effects of electron correlation and interferences in between different ionization and dissociation channels. The field–molecule interaction is described within the dipole approximation, which is valid for the wavelengths used here. In brief, we numerically solve the TDSE by expanding the time-dependent wave function in a basis of the vibronic eigenstates of the molecule (H_2 or D_2). The vibronic states are obtained within the Born–Oppenheimer approximation, i.e., they are written as products of electronic and vibrational wave functions. The molecular Hamiltonian and the laser field couple these states when the expansion is introduced in the TDSE. The bound and continuum electronic states are described by using a Feshbach-like method (see details in refs. 4–6 and references therein). In this method, the electronic states results form configuration interaction (CI) calculations restricted to different subspaces. Each configuration in the CI expansion is written as an antisymmetrized product of H_2^+ orbitals described as monocentric expansions in terms of B-splines and spherical harmonics. In the present problem, the vibrational (dissociative) wave functions are represented in a basis of 300 B-splines inside a box of 14 a.u., and the radial part of the molecular orbitals in a basis of 180 B-splines inside a box of 60 a.u. and spherical harmonics up to $l = 16$. We are focused on the detection of the fragments from the molecules aligned parallel to the laser polarization axis, so our present calculations only include states of Σ symmetry.

To model the nuclear wave packet (NWP) motion generated by the combined VUV + phase-locked IR pulse on a given electronic state (Fig. 4 *A* and *B* and Figs. S4 and S5), we solved the nuclear TDSE by using the potential energy associated with that electronic state and the initial boundary condition:

$$\psi(R, t=t_0) = \sum_k c_k \chi_k(R) \exp(-i\varepsilon_k t_0),$$

where c_k is the amplitude resulting from TDSE calculations as those described above for H_2, but in which only the combined VUV + phase-locked IR pulse is used (i.e., no IR probe); χ_k is the kth vibrational wave function in the chosen electronic state; ε_k is the corresponding vibronic energy; and t_0 is the time just at the end of the combined VUV + phase-locked IR pulse. To account for the fact that the D_2 reduced mass is twice as large as that of H_2, the time in the above equation has been rescaled by a factor $\sqrt{2}$.

Fig. S3 represents a more detailed version of Fig. 2, showing the theoretical yields as well as the kinetic energy of the D^+ ions and the electrons. The photoelectron energies shown in Fig. S3*A* confirm that the two interfering electronic wave packets ($9\omega + \omega$ vs. $11\omega - \omega$) are indeed responsible for the total yield oscillation with the main periodical signal being just above the ionization threshold (10ω). Also, the proton kinetic energy shown in Fig. S3*B* indicates that due to the shorter IR/VUV pulses used in our calculations, the dissociation happens at shorter internuclear separations (higher dissociation kinetic energy), where the pulses are still temporally overlapped, and where quantum interferences play an important role.

In Figs. S4 and S5, we show the nuclear wave packet dynamics calculations for the VUV central energies shown in Fig. 4, but for several other excited states populated by the VUV harmonics. For the B state at 784 nm (Fig. S4*A*), two periodicities appear: ∼30 fs (small internuclear separation R), corresponding to population of low vibrational states of the B state by 7ω, and ∼ 80 fs (large R), which is probed by the one-step B mechanism. When the photon energy increases (i.e., 760 nm; Fig. S4*B*), the vibration in the B potential at large R has a larger period due to excitation to higher vibrational levels in the Franck–Condon region, and its probability is smaller due to dissociation.

To observe these periodicities, we performed a Fourier transform of the time evolution of the nuclear wave packets shown in Fig. S4. The results are shown in Fig. S6. The predicted periodicities ∼30 and 80 fs are present for the B state. A zoom over long internuclear distances of the Fourier transforms of the B state (shown in Fig. S6 *A* and *B*) are shown in Fig. S7. The vibration in the EF potential can also be seen at 784 nm (Figs. S4*C* and S6*C*), but it is even more clearly visible for 760-nm wavelengths (Figs. S4*D* and S6*D*); this is because, at 784 nm, the nuclear wave packet is mainly created in the inner and outer wells of the EF potential energy curve, with very little probability of tunneling through the potential barrier located at R ∼3.5 a.u. Thus, the corresponding vibrational periods are ∼20–30 fs at small R. In contrast, at 760 nm (Fig. S4*D*), the nuclear wave packet tunnels efficiently through the barrier and moves along the EF potential energy curve, with a vibrational period that is close to that observed in the B state. Note that the populations are 20× smaller in Fig. S4 *C* and *D* than in *A* and *B*.

Finally, in Fig. S8 we show the extended Fourier transforms, corresponding to the data shown in Fig. 4. All structures associated with periodicities larger than 40 fs are explained in the caption of Fig. 4 and in the main text. Fig. S7 also shows the appearance of peaks associated with periodicities in the range 20–40 fs, which correspond to nuclear wave packets generated by the seventh harmonic in the B state, by the $7\omega + \omega$ and $9\omega - \omega$ in the inner (and likely outer) wells of the EF state, and by the 11ω and 13ω on the $1s\sigma_g$ state of D_2^+.

1. Rundquist A, et al. (1998) Phase-matched generation of coherent soft X-rays. *Science* 280(5368):1412–1415.
2. Ranitovic P, et al. (2011) Controlling the XUV transparency of helium using two-pathway quantum interference. *Phys Rev Lett* 106(19):193008.
3. Ranitovic P, et al. (2010) IR-assisted ionization of helium by attosecond extreme ultraviolet radiation. *New J Phys* 12:013008.
4. Palacios A, Bachau H, Martín F (2006) Enhancement and control of H2 dissociative ionization by femtosecond VUV laser pulses. *Phys Rev Lett* 96(14):143001.
5. Sanz-Vicario JL, Bachau H, Martin F (2006) Time-dependent theoretical description of molecular autoionization produced by femtosecond XUV laser pulses. *Phys Rev A* 73: 033410.
6. Palacios A, Bachau H, Martin F (2007) Excitation and ionization of molecular hydrogen by ultrashort VUV laser pulses. *Phys Rev A* 75:013408.
7. Kelkensberg F, et al. (2011) Attosecond control in photoionization of hydrogen molecules. *Phys Rev Lett* 107(4):043002.
8. Sansone G, et al. (2010) Electron localization following attosecond molecular photoionization. *Nature* 465(7299):763–766.

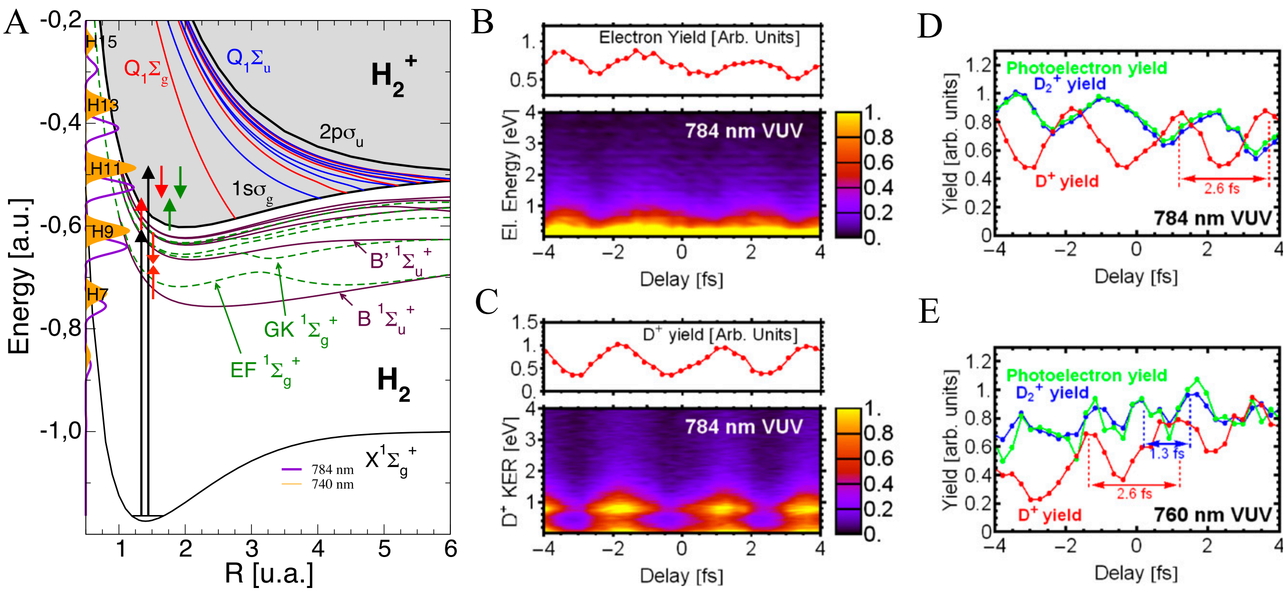

Fig. S1. (*A*) Detailed potential energy surfaces of the H_2 neutral and the H_2^+ ground and excited states (identical to those of D_2 and D_2^+). The red and green arrows represent driving and probing IR pulses, respectively. (*B*) The photoelectron yield modulation results from the laser-induced interference of the electron wave packets created by the attosecond VUV frequency comb. The IR laser wavelength was 784 nm, and the VUV photons were 7ω, 9 ω, 11 ω, etc. (*C*) The D^+ dissociative yield modulation results from the intensity modulation of the interfering driving and probing IR pulses. (*D*) A comparison of the D^+/e^- yields reveals that the ionization and dissociative dynamics are out of phase. (*E*) By increasing the energy of the VUV photons, we change the electron-yield modulation period from full to half-optical cycle periodicity.

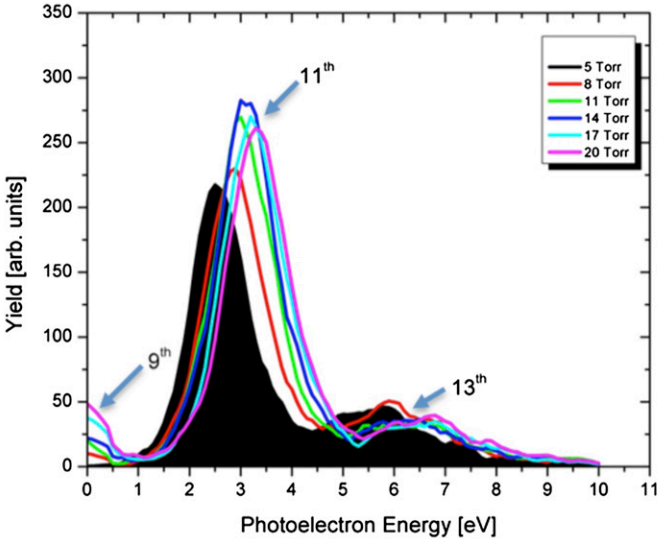

Fig. S2. Fine-tuning of the VUV HHG energy by phase matching. Photoelectron energies from Ar ionized by a VUV HHG comb show how increasing the Xe gas pressure can blue-shift the HHG peaks while keeping the IR wavelength fixed.

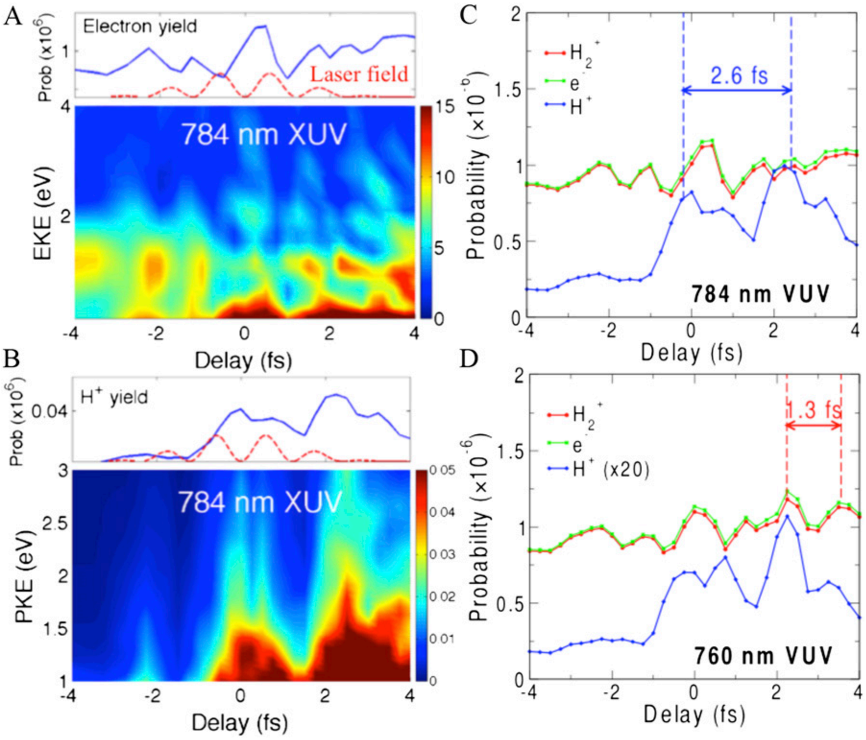

Fig. S3. Calculated electron (*A*) and proton (*B*) kinetic energies (PKE) obtained by solving the TDSE for a hydrogen molecule in the presence of 5-fs VUV and IR pulses. (*C* and *D*) The calculated H_2^+/e^- yields vs. H^+ yields show the same trend as seen in the experimental data—namely, as the central energy of the VUV frequency comb is blue-shifted from 784 nm to 760 nm, the total ionization yield clearly switches from full to half-a-cycle periodicity.

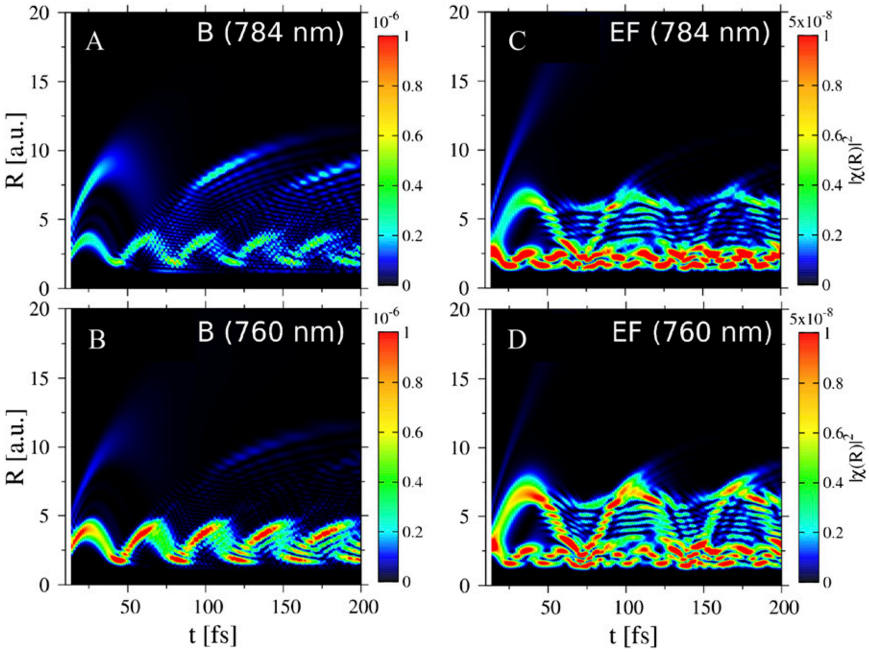

Fig. S4. Time evolution of the nuclear wave packets created in the B $^1\Sigma_u^+$ (*A* and *B*) and EF $^1\Sigma_g^+$ potential energy surfaces (*C* and *D*) by the combined VUV and IR fields, for 784 nm (*Upper*) and 760 nm (*Lower*) IR wavelengths.

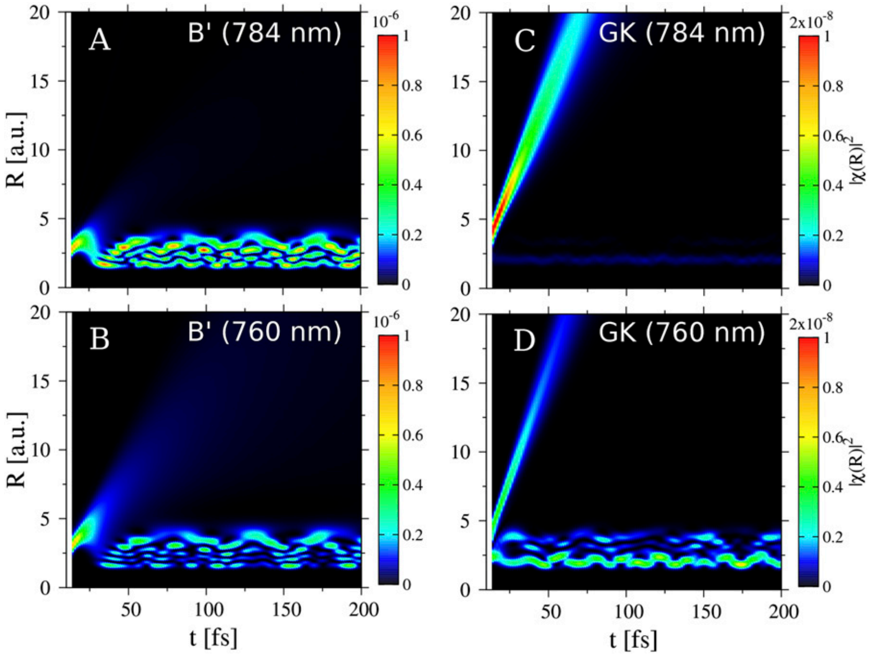

Fig. S5. Same as in Fig. S4 but for the B′ (*A* and *B*) and GK (*C* and *D*) states. The lowest vibrational states of the B′ state are populated by the ninth harmonic (*A*). For higher photon energies (760 nm), the VUV absorption leads to dissociation (*B*). Excitation to the GK state leads primarily to dissociation (*C*), whereas for higher frequency, the low vibrational states are also populated (*D*). Note that the populations are 50× smaller in *C* and *D* than in *A* and *B*.

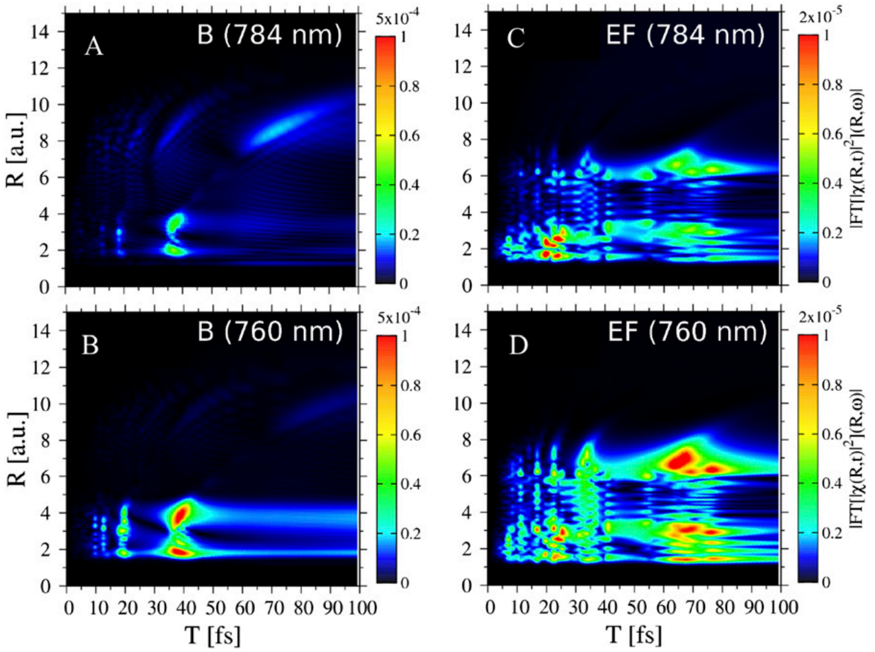

Fig. S6. (*A*–*D*) The 2D Fourier transforms of the nuclear wave packets shown in Fig. S4.

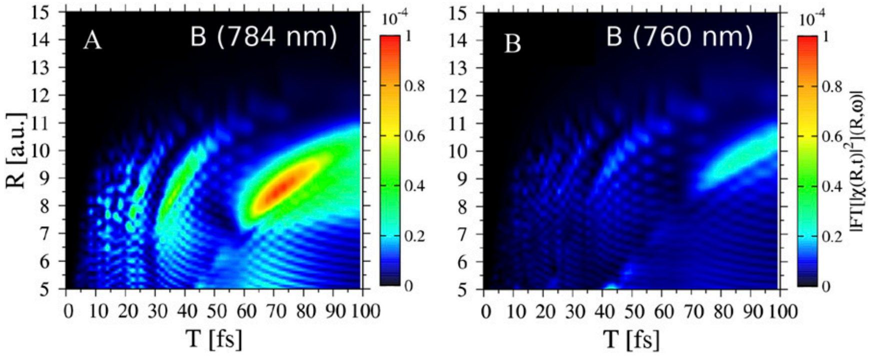

Fig. S7. (*A* and *B*) Zoom-in for large internuclear distances of the 2D Fourier transforms of the nuclear wave packets shown in Fig. S6 *A* and *B*.

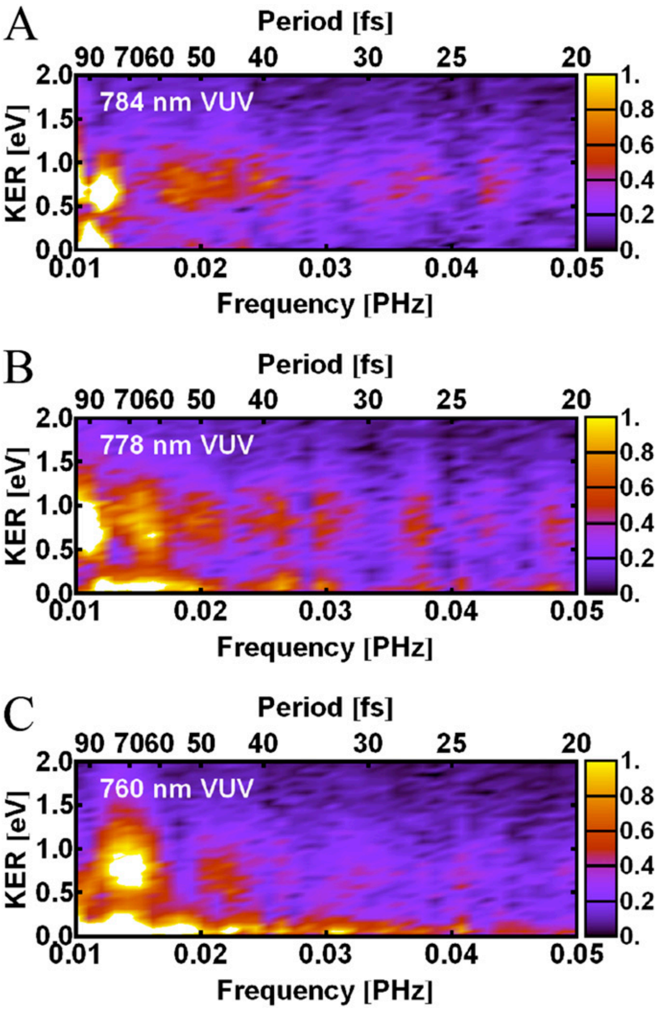

Fig. S8. (*A*–*C*) Extended 2D Fourier transforms of the proton kinetic energy releases shown in Fig. 4 *F*–*H*, as a function of the central energy of the VUV pulse.